Korean J. Chem. Eng., 37(3), 556-562 (2020)
DOI: 10.1007/s11814-020-0474-9

pISSN: 0256-1115
eISSN: 1975-7220

Which electrode is better for biomass valorization: $Cu(OH)_2$ or CuO nanowire?

Hoang Minh Pham[*,,‡], Myung Jong Kang[*,‡], Kyung-An Kim[*,‡], Chang Gyu Im[***], Sung Yeon Hwang[*,**,†], and Hyun Gil Cha[*,†]**

*Bio-based Chemistry Research Center, Korea Research Institute of Chemical Technology (KRICT), Ulsan 44429, Korea
**Advanced Materials and Chemical Engineering, University of Science and Technology (UST), Daejeon 34113, Korea
***Department of Materials & Chemical Engineering, Hanyang University, Ansan 15588, Korea
(*Received 16 September 2019 • accepted 25 December 2019*)

Abstract−2,5-furandicarboxylic acid (FDCA), one of the key building block for replacing petroleum-derived terephthalic acid, is utilized as the source of bioplastics, pharmaceuticals. Herein, free-standing $Cu(OH)_2$ and CuO nanowires as electrode were examined to disclose the effects of crystal structure and chemical formation based on copper oxide in electrocatalytic 5-Hydroxymethylfurfural (HMF) oxidation to FDCA in 0.1 M KOH solution. We introduced on three-dimensional copper foam (CuF) with high porosity as copper source and substrate with high conductivity free-standing $Cu(OH)_2$ and CuO nanowires (NWs) on the substrate by inorganic polymerization and calcination for electrochemical HMF oxidation. This was enabled by square-planar coordination (σ_{x2-y2}) of Cu^{2+} ions in (001) crystal faces of $Cu(OH)_2$ crystal. As a result of stacking with hydrogen bonds, free-standing $Cu(OH)_2$ NWs on the substrate was formed. There was no change in the morphology of the nanowire arrays, but the active sites from a plane area per surface-exposed Cu atoms by transformation of $Cu(OH)_2$ to CuO NWs increased.

Keywords: $Cu(OH)_2$ Nanowire, CuO Nanowire, Inorganic Polymerization, Electrocatalytic Oxidation, 5-Hydroxymethylfurfural

INTRODUCTION

Because of the harmful ramifications of using petroleum as a source of energy and carbon-based materials on the environment, recycled waste materials are increasingly being regarded as eco-friendly renewable energy resources for value-added materials [1]. In this respect, biomass conversion, in which bio-based wastes are converted to other valuable monomers for carbon-based products, is the best alternative means of replacing fossil-fuel-derived carbon with bio-based carbon [2]. The biorefinery process enables the utilization of carbon stored in organic materials as a fuel and industrial carbon source [3]. Among the various kinds of biorefinery process intermediates, 5-hydroxymethylfurfural (HMF), a furan-containing intermediate, is one of the most important because it is used as a precursor for various plastics, liquid fuels, and pharmaceuticals [4]. Moreover, the oxidized form of HMF, 2,5-furandicarbocylic acid (FDCA), can replace the petroleum-derived terephthalic acid, which is used in the preparation of polyurethanes, polyamides, polyesters, and polyethylene. Therefore, the oxidation of HMF to FDCA is a core process in the biomass refinery [5].

Despite the importance of this process, the limitations of the pristine heterogeneous catalytic process for HMF oxidation have not been addressed. Specifically, this process requires high oxygen pressure during the reaction and noble metal catalysts such as Pt, Au, Pd, Ru, or several sorts of alloys [6]. Moreover, unintended by-products, such as 5-hydroxymethyl-2-furancarboxylic acid (HMFCA), 2,5-diformylfuran (DFF), and 5-formylfuran-2-carboxylic acid (FFCA), are formed [7]. Electrochemical oxidation of HMF to FDCA has gained increasing attention because the process can be performed by electricity under room temperature and atmospheric conditions [8]. However, in addition to noble metal electrodes [9], a redox mediator (e.g., 2,2,6,6-tetramethylpiperidin-1-yl)oxyl or N-methylmorphilone N-oxide) [10] is required to get high efficiency and high selectivity. To overcome the disadvantages of electrochemical HMF oxidation, utilizing nanostructured transition-metal-based electrodes, such as TiO_2 [11], Co-P [12], MnO_2 [13], Ni-W_2C [14], $NiCo_2O_4$ [15] and heterogeneous composite materials [16,17] has been reported to exhibit improved catalytic efficiency.

In this work, we employed $Cu(OH)_2$ and CuO nanowires (NWs) as electrode, which was directly grown on conductive copper foam (CuF) with high porosity as substrate without a sacrificial template for the electrochemical oxidation of HMF into FDCA. Cu, one of the most abundant transition metals on earth, can exist in various electronic states that are suitable for electron transfer from HMF to the electrode during oxidation. The catalytic performance of $Cu(OH)_2$ and CuO NWs freely standing on CuF electrodes was evaluated and rationalized.

EXPERIMENTAL

1. Materials

HMF (>99%), HMFCA (97%), FDCA (97%) and Nafion 115 membrane were purchased from Sigma-Aldrich). DFF (97%) and FFCA (>98.0%) were purchased from TCI Chemicals. $(NH_4)_2S_2O_8$ (>99%), KOH (95.0%), NaOH (98.0%), HCl (35-37%) and H_2SO_4

†To whom correspondence should be addressed.
E-mail: crew75@krict.re.kr, hgcha@krict.re.kr
‡These authors contributed equally to this work.
Copyright by The Korean Institute of Chemical Engineers.

(97%) were purchased from Samchun Chemicals. CuF was purchased from MTI Korea Ltd. Deionized water (18 MΩ/cm) produced by the Milli-Q Integral 10 water purification system (Millipore) was used in following experiments. All chemicals were used as received without further purification.

2. Preparation of $Cu(OH)_2$ and CuO NWs/CuF Electrodes

$Cu(OH)_2$ and CuO NWs/CuF were prepared following the literature procedure with minor modification [18]. CuF was cleaned by using 1 M HCl solution, then rinsed several times with deionized water and ultra-sonicated in the same for 10 min to remove the surface oxide. Subsequently, a piece ($1\times1.5\ cm^2$) of CuF was immediately immersed in 20 mL of an etchant solution containing 0.125 M $(NH_4)_2S_2O_8$ and 2.5 M NaOH at room temperature for 20 min. The resulting $Cu(OH)_2$ NWs/CuF, which color is a sky blue, was removed from the solution and washed with deionized water several times and dried under N_2 flow. To obtain CuO NWs/CuF, $Cu(OH)_2$ NWs/NF was calcined at 180 °C under air for 1 h.

3. Electrocatalyst Testing

Catalytic activity of the electrodes in HMF oxidation was performed by linear sweep voltammetry (LSV) measurement using Bio-Logic VSP potentiostat/galvanostat with three-electrode system in 0.1 M KOH (pH 13) with and without 5 mM HMF aqueous solution in an undivided cell. $Cu(OH)_2$ and CuO NWs/CuF were used as working electrode, while Pt mesh was used as counter electrode. Hg/HgO/1 M KOH reference electrode was used without stirring. The potential was swept from the open circuit potential (OCP, V_{oc}) to positive direction with a rate of 10 mV/s. The potential used for electrochemical measurements was converted to the reversible hydrogen electrode (RHE) by the following equation and reported.

$$E_{RHE}\ (V)=E_{Hg/HgO}\ (V)+E_{Hg/HgO}\ (\text{reference})+0.0591\ V\times pH\ (\text{at } 25\ ^{\circ}C)$$

($E_{Hg/HgO}$ (reference, 1 M KOH)=0.098 V vs. NHE at 25 °C)

Electrochemical impedance spectroscopy (EIS) analysis was performed in the range of 100 kHz to 100 mHz with 10 mV of amplitude. For this analysis, 10 mM of HMF solution in 0.1 M KOH was used as electrolyte, and an external bias potential of 1.65 V (vs. RHE) was applied.

4. Catalytic Reactions

Before electrocatalytic oxidation of HMF, the $Cu(OH)_2$ NWs/CuF and CuO NWs/CuF electrode was oxidized by sweeping from V_{oc} to 1.2 V vs. Hg/HgO at room temperature without stirring in 0.1 M KOH electrolyte solution, with a scan rate of 10 mV/s. Electrocatalytic oxidation of HMF was performed in an H-type divided electrochemical cell with a Nafion 115 membrane separating the anodic from the cathodic compartment. As described above, $Cu(OH)_2$ NWs/CuF and CuO NWs/CuF was as working electrode (geometric area of 3 cm^2). For the counter electrode, Pt mesh was used and immersed in the cathodic compartment (14 mL of 0.1 M KOH solution) and Hg/HgO reference electrode was immersed in the anodic compartment containing 14 mL of 0.1 M KOH solution with 5 mM HMF. Experiments were conducted at room temperature using a different constant potential for each electrode. The solution was stirred with 700 rpm during the experiments. The uncompensated IR drop was not corrected in all electrochemical analyses reported in this study.

The concentration of consumed HMF and produced product in the anodic compartment was measured by high performance liquid chromatography (HPLC, YL9100 with UV detector, 265 nm for detecting), with a 10 μL of solution taken from the cell during and after the reaction. 1 h of equilibration period was performed before injection. 5 mM of sulfuric acid was used as the mobile phase with the 0.5 ml/min of flow rate at 65 °C within the isocratic mode. The standards and sample (10 μL in volume) were injected directly into a Hi-Plex H column (Agilent Technologies, 300 mm×7.7 mm). The qualification and quantification of the products were performed by calibration curves (0.999 of correlation coefficient) by applying a known concentration of standard solution. Triplicate experiments were performed and the average value was used for all HPLC data in the report.

The amount of produced hydrogen in cathodic compartment during HMF oxidation reaction was measured by gas chromatography (GC, Agilent 7890B with thermal conductivity detector) with Agilent DB-624 column. The qualification and quantification of gaseous products were determined and calculated from calibration curves (0.999 of correlation coefficient), measured by concentration-known standard gas mixture.

The HMF conversion, yields of the oxidation product and faradic efficiency (FE) for the production of FDCA were calculated by using Eqs. (1)-(3) where F is the Faraday constant.

$$\text{Conversion}\ (\%)=\frac{(\text{mol of HMF consumed})}{(\text{mol of initial HMF})}\times100\ (\%), \tag{1}$$

$$\text{Yield}\ (\%)=\frac{(\text{mol of product formed})}{(\text{mol of initial HMF})}\times100\ (\%), \tag{2}$$

$$\text{FE}\ (\%)=\frac{(\text{mol of FDCA formed}\times6\times\text{F})}{(\text{total charge passed})}\times100\ (\%), \tag{3}$$

5. Characterizations

The surface morphology and elemental composition were evaluated using a scanning electron microscope (SEM, Tescan Mira3, operated in 15 kV of an accelerating voltage) equipped with an energy dispersive spectrometer (EDS, Thermo-Fisher EDS detector at 15 kV). The crystal structures were measured by X-ray diffraction (XRD, Rigaku D/MAX 2550 diffractometer, Cu K_α radiation generator, between 10° and 80°) and high resolution transmittance electron microscopy (HR-TEM, JEOL-2100 F). The TEM sample was prepared by dispersing the nanowires, scratched off from the electrode, in ethanol under ultra-sonication for 10 min, and drop-casting an amount of 5 μL of the suspension onto a carbon coated copper grid. The atomic binding state and structures of the samples were investigated by X-ray photoelectron spectroscopy (XPS, with Al K_α source), (K-alpha, Thermo UK).

RESULTS AND DISCUSSION

1. Preparation and Growth Mechanism of $Cu(OH)_2$ and CuO NWs/CuF Electrode

Preparation of $Cu(OH)_2$ and CuO NWs/CuF is illustrated in Scheme 1. It was grown as nanowires on CuF avoiding the use of a sacrificial template [19]. This method prevents not only the increase in contact resistance between Cu-based NWs and the conductive

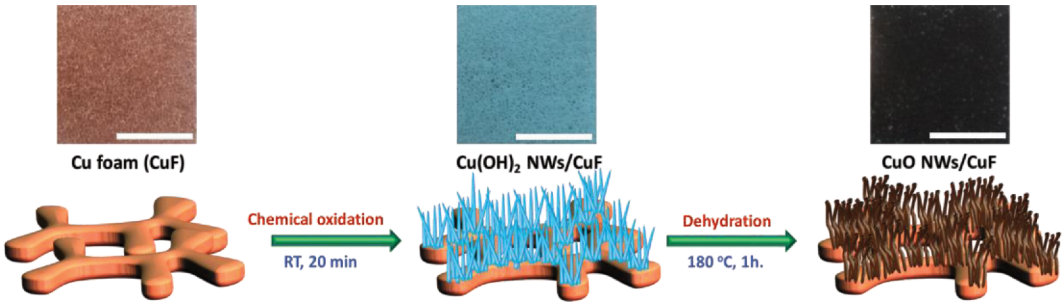

Scheme 1. Optical image and scheme of fabrication methods for $Cu(OH)_2$ and CuO NWs/CuF (inset: optical image of CuF, $Cu(OH)_2$ and CuO NWs/CuF; all scale bar is 0.5 cm).

substrate, but also disturbing the diffusion of electrolyte, thereby resulting in enhanced catalytic performance [20]. The free-standing $Cu(OH)_2$/CuF and CuO NWs/CuF follows inorganic polymerization reaction [21] in alkaline conditions as follows:

$$Cu+4\ OH^- + (NH_4)_2S_2O_8 \rightarrow Cu(OH)_2 + 2\ NH_3(g) + 2\ SO_4^{2-} + 2\ H_2O \quad (4)$$

$$Cu(OH)_2 \rightarrow CuO + H_2O \quad (5)$$

The formed $Cu(OH)_2$ in Eq. (4) can be converted into CuO via dehydration (Eq. (5)).

2. Morphology and Structural Characterization of $Cu(OH)_2$ and CuO NWs/CuF Electrode

The surface morphologies of $Cu(OH)_2$ and CuO NWs/CuF studied by SEM are shown in Fig. 1. A dense and uniform layer of $Cu(OH)_2$ NWs completely covers the CuF, which has a length of around 10 μm (Fig. 1(a) and 1(b)). A higher magnification shows

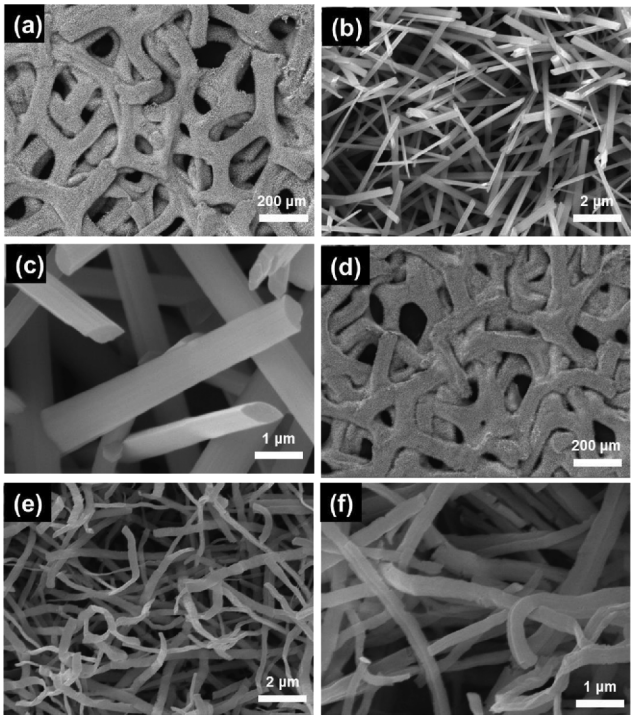

Fig. 1. SEM images of $Cu(OH)_2$ NWs/CuF ((a)-(c)) and CuO NWs/CuF ((d)-(f)).

that the smooth NWs have a diameter in the range of 200-300 nm (Fig. 1(c)). EDS analysis reveals that $Cu(OH)_2$ NWs/CuF is composed 36.74% Cu and 63.26% O for an atomic ratio of 1 : 2 (Fig. S1(a)), which matches the chemical formula well. After being calcined under air at 180 °C, the obtained CuO NWs still compactly and fully covered the CuF, as shown in Fig. 1(d)-(f). However, compared with the smooth and straight $Cu(OH)_2$ NWs (Fig. 1(c)), the CuO NWs are curled and have wrinkles on the surface (Fig. 1(f)) owing to the removal of water from $Cu(OH)_2$ NWs [22]. EDS analysis of CuO NWs/CuF shows an elemental composition of 49.88% Cu and 50.12% O for an atomic ratio approximately 1 : 1 (Fig. S1(b)), which also matches the chemical formula well.

To investigate the crystal structures of $Cu(OH)_2$ NWs and CuO NWs/CuF, XRD patterns were obtained and are shown in Fig. S2. The XRD pattern of $Cu(OH)_2$ NWs/CuF in Fig. S2(a) presents the typical diffraction peaks at 2θ=33.9°, 35.6°, 38.1°, 39.6° and 53.2°, which can be assigned to the (002), (111), (022), (130) and (150) planes, respectively, of the orthorhombic phase of $Cu(OH)_2$ (JCPDS card no. 13-0420) [23]. Three additional diffraction peaks with high intensity at 2θ=43.1°, 50.2° and 73.9° are indexed to the (111), (002) and (220) planes, respectively, of the metallic CuF (JCPDS card no. 04-0836) [24]. Except for these signals from the CuF, no other impurity peaks are observed in $Cu(OH)_2$ NWs/CuF, which indicates that high crystallinity and purity were obtained after the oxidation step. Additionally, CuO NWs/CuF was transformed by calcination of $Cu(OH)_2$ NWs/CuF, the two characteristic diffraction peaks of CuO positioned at 2θ=35.6° and 38.8° are observed in the XRD pattern of CuO NWs/CuF, assigned as the (11-1) and (111) planes, respectively, of the monoclinic phase of CuO (JCPDS card no. 48-1548) in Fig. S2(b) [25]. This suggests that CuO NWs/CuF was successfully obtained by dehydration of $Cu(OH)_2$ to CuO by calcination under air condition. The XRD patterns of $Cu(OH)_2$ and CuO NWs/CuF still present strong characteristic signals from the CuF. This indicates that the $Cu(OH)_2$ and CuO NWs were directly grown on the surface of CuF with good conductivity as current collector [26].

The crystal structure of $Cu(OH)_2$ and CuO NWs/CuF electrode was further investigated by TEM. $Cu(OH)_2$ NWs have a fine nanowire structure and the EDS line profiling on the TEM image matches the atomic composition of $Cu(OH)_2$ well (Fig. 2(a)). In HR-TEM image, a clear lattice fringe is observed with several domains of particles having the (002) plane structure, which has a d-spacing

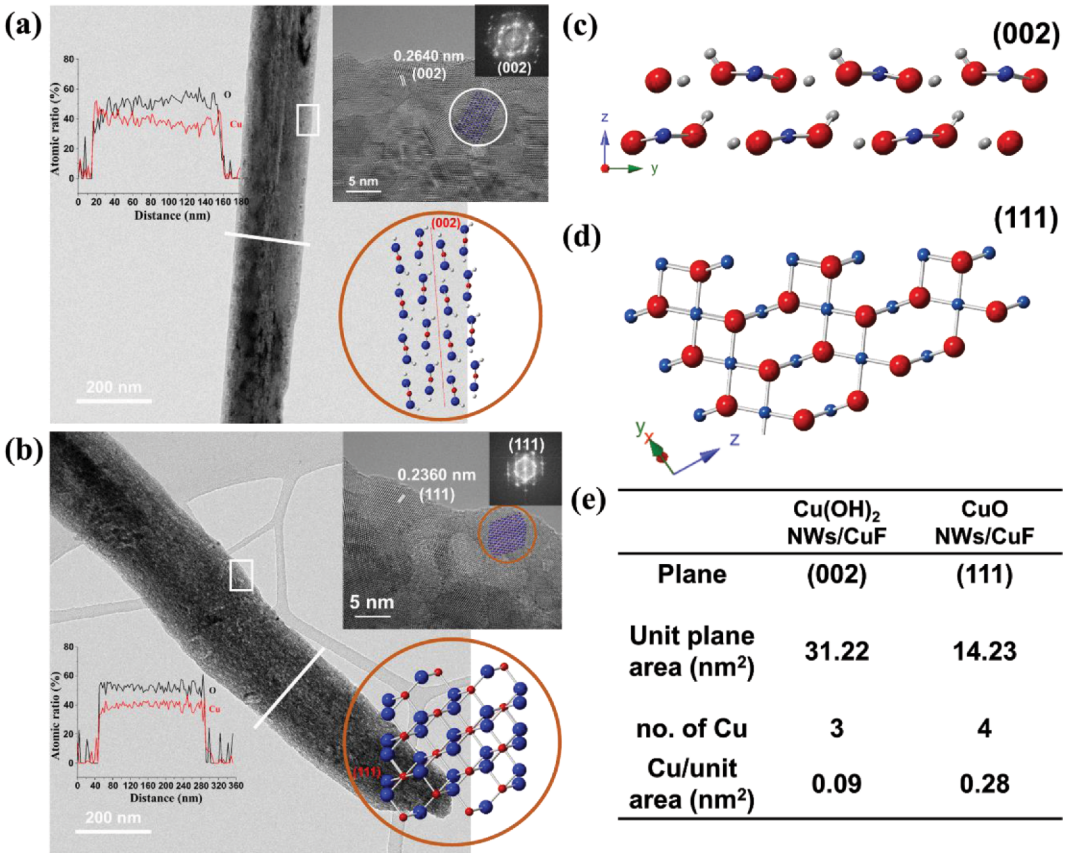

	$Cu(OH)_2$ NWs/CuF	CuO NWs/CuF
Plane	(002)	(111)
Unit plane area (nm^2)	31.22	14.23
no. of Cu	3	4
Cu/unit area (nm^2)	0.09	0.28

Fig. 2. TEM images, TEM-EDS line profiling, HR-TEM images with FFT pattern and crystal structure of (a) $Cu(OH)_2$ and (b) CuO NWs/CuF. Surface structure of (c) $Cu(OH)_2$ and (d) CuO NWs/CuF. (e) Table of unit plane area and Cu atom per unit area (Blue: Cu, Red: O and Gray: H atoms).

of 0.264 nm. As shown in Fig. 2(b), CuO NWs also have fine nanowire structure and the EDS line profiling of the atomic ratio is consistent with the atomic composition of CuO. In the HR-TEM image, the clear lattice fringe of the (111) plane with a d-spacing of 0.236 nm and several domains of particles is observed. Based on the fast Fourier transform (FFT) patterns, although $Cu(OH)_2$ and CuO NWs consist of randomly stacked particles, they align in a direction to form the nanowire structure. In addition, lattice parameters are consistent with the highest peak in the XRD analysis. The surface molecular structures of $Cu(OH)_2$ and CuO NWs/CuF are shown in Fig. 2(c) and 2(d), respectively. Since the metal atoms of metal oxide based electrocatalysts become an active site during electrochemical reaction, the unit cell structure modeling of $Cu(OH)_2$ and CuO was performed [15,27]. Based on the unit cell structure modeling and calculation, CuO (111) plane has smaller unit plane area of 14.23 nm^2 than (002) plane of $Cu(OH)_2$, which is 31.22 nm^2. Considering number of surface exposed Cu atoms within unit plane area, CuO (111) plane has 0.28 number of Cu atom in square nanometer, while the $Cu(OH)_2$ (002) plane has 0.09 number of Cu atoms in square nanometer (Fig. 2(e)).

XPS was used to investigate chemical binding states of $Cu(OH)_2$ NWs/CuF and CuO NWs/CuF shown in Fig. 3. The Cu 2p XPS spectrum of $Cu(OH)_2$ NWs/CuF presents two peaks at 934.79 and 954.49 eV corresponding to the binding energies of Cu $2p_{3/2}$ and Cu $2p_{1/2}$, respectively, which matches those reported for $Cu(OH)_2$ [13]. Two shake-up satellite peaks at 942.38 and 962.38 eV are clearly observed and can be respectively assigned to Cu $2p_{3/2}$ and Cu $2p_{1/2}$ (Fig. 3(a)). The results demonstrate the existence of Cu^{2+} on the surface of $Cu(OH)_2$ NWs/CuF [28]. This is further confirmed by the O 1s XPS spectrum in Fig. 3(b). The main peak of O 1s at 531.88 eV follows the binding energy of the hydroxyl group of $Cu(OH)_2$. The other peak at the higher binding energy of 533.54 eV can be assigned to oxygen chemisorbed on the surface [29]. On the other hand, the Cu 2p XPS spectrum of CuO NWs/CuF shows that Cu $2p_{3/2}$ and Cu $2p_{1/2}$ have lower binding energies (934.09 and 953.77 eV, respectively) than those in $Cu(OH)_2$ NWs/CuF [30]. Fig. 3(d) shows that the O 1s XPS spectrum of CuO NWs/CuF has a main peak at 529.78 eV due to the Cu-O bond in the CuO crystal lattice and another peak at 531.26 eV attributable to hydroxyl groups adsorbed on the surface [26].

This work provides a simple and efficient process for the preparation of $Cu(OH)_2$ and CuO NWs/CuF as electrode for electrochemical HMF oxidation. In addition, the crystal structure can be transformed from $Cu(OH)_2$ to CuO by dehydration reaction. This change will increase the number of surface-exposed Cu atoms in unit plane area and decrease binding energies in Cu $2p_{3/2}$ and Cu $2p_{1/2}$ due to high portion of Cu^{2+} species, which implies better electron transport and high rate of electrochemical HMF oxidation.

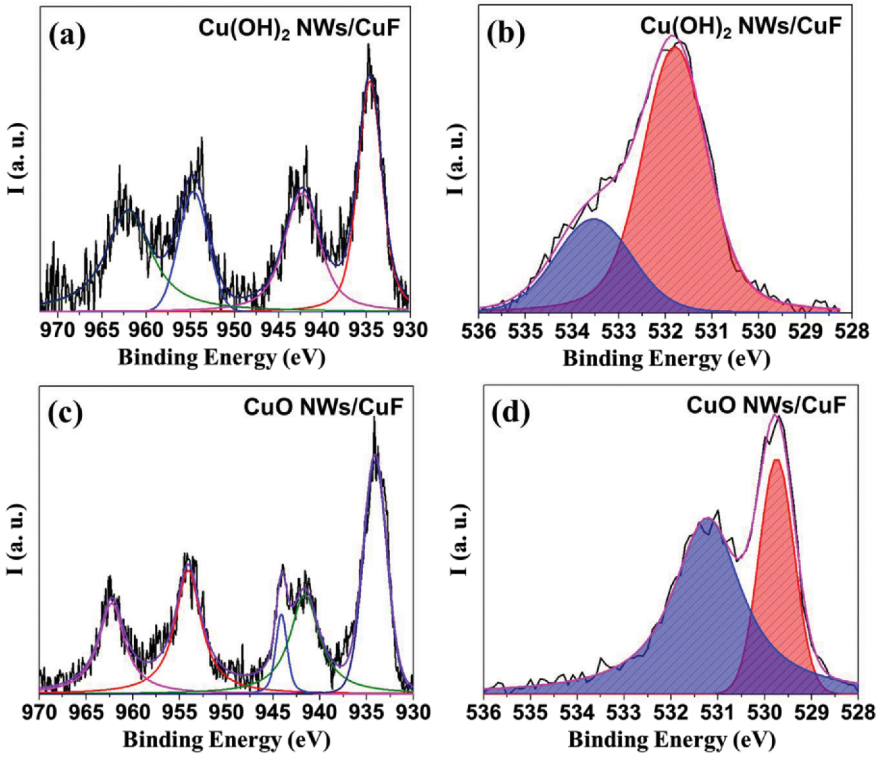

Fig. 3. XPS spectra of $Cu(OH)_2$ and CuO NWs/CuF, respectively. (a), (c) Cu 2p, (b), (d) O 1s.

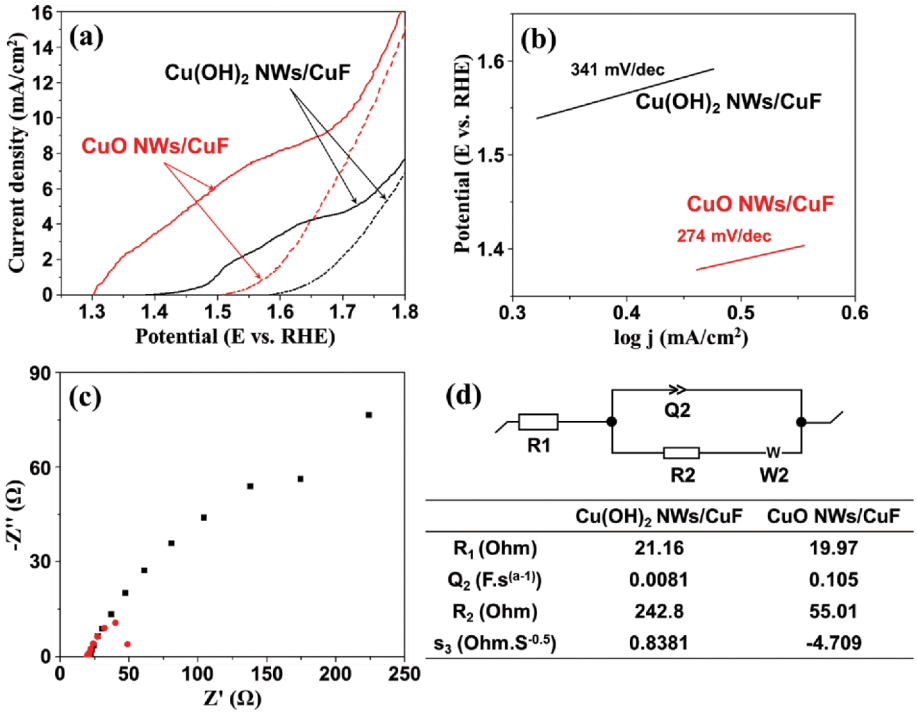

	$Cu(OH)_2$ NWs/CuF	CuO NWs/CuF
R_1 (Ohm)	21.16	19.97
Q_2 ($F.s^{(a-1)}$)	0.0081	0.105
R_2 (Ohm)	242.8	55.01
s_3 ($Ohm.S^{-0.5}$)	0.8381	-4.709

Fig. 4. (a) LSV curves, (b) Tafel plots, (c) Nyquist plots, (d) Scheme of suggested equivalent circuit for fitting and table of each fitted parameters of $Cu(OH)_2$ (black) and CuO NWs/CuF (red) electrode.

3. Electrocatalytic behavior of $Cu(OH)_2$ and CuO NWs/CuF Electrode in HMF Oxidation

To evaluate the electrocatalytic activity of the $Cu(OH)_2$ and CuO NWs/CuF electrodes for HMF oxidation, LSVs were performed using a 0.1 M KOH electrolyte solution in the presence of 5 mM HMF and the results are shown in Fig. 4(a). Without HMF, the

onset potential of $Cu(OH)_2$ and CuO NWs/CuF electrodes for water oxidation showed 1.6 V and 1.5 V vs. RHE, respectively. When HMF was added, a shift of the anodic current onset potential of each electrode toward the negative direction and a significant increase in the current density were observed. To be specific, $Cu(OH)_2$ NWs/CuF electrode showed more positive onset potential and lower current density compared to CuO NWs/CuF electrode. It means that CuO NWs/CuF has the better catalytic activity for HMF oxidation. For more detailed investigation, the electron transfer rate of the $Cu(OH)_2$ and CuO NWs catalysts in HMF oxidation was compared by examining their corresponding *Tafel* slopes (Fig. 4(b)). Calculated *Tafel* slopes of $Cu(OH)_2$ and CuO NWs/CuF are 341 and 274 mV/dec, respectively. The results indicate that CuO NWs/CuF electrode exhibits the fastest HMF oxidation and requires the lowest potential for increasing the HMF oxidation rate.

To further investigate the higher efficiency for HMF conversion to FDCA of CuO NWs/CuF, EIS was performed using 10 mM HMF in 0.1 M KOH solution and an applied external bias potential of 1.65 V. The Nyquist plots of $Cu(OH)_2$ and CuO NWs/CuF show the typical semicircle in the high frequency region, which is regarded as the charge transfer region of the electrochemical cell (Fig. 4(c)). The equivalent circuit for fitting the Nyquist plot is shown in Fig. 4(d) [31]. It consists of the series resistance (R_1), double-layer capacitance (Q_2), Warburg resistance (W_2), and charge transfer resistance (R_2). The fitted parameters are shown in Fig. 4(d). Particularly, the crucial parameter in the kinetics of the catalytic reaction is R_2, which is 242.8 and 55.01 Ω for $Cu(OH)_2$ and CuO NWs/CuF, respectively. The smaller R_2 of CuO NWs/CuF is consistent with its higher HMF oxidation current density compared with that of $Cu(OH)_2$ NWs/CuF, and indicates fast electron transfer rate on this electrode during electrocatalytic HMF oxidation. These results clearly indicate that CuO NWs/CuF has the best kinetic and thermodynamic properties for HMF oxidation.

4. Electrocatalytic Performance of $Cu(OH)_2$ and CuO NWs/CuF

Simultaneous electrochemical HMF oxidation and water reduction are summarized below [10]:

$$\text{anodic reaction: } HMF+2H_2O \rightarrow FDCA+6H^++6e^- \quad (15)$$

$$\text{cathodic reaction: } 6H^++6e^- \rightarrow 3H_2 \quad (16)$$

$$\text{overall reaction: } HMF+2H_2O \rightarrow FDCA+3H_2 \quad (17)$$

To monitor conversion, yields, reaction time and FE of FDCA, oxidation was performed by applying a constant potential using an H-type electrochemical cell summarized in Table S1.

$Cu(OH)_2$ NWs/CuF was tested as anode for HMF oxidation by applying a constant potential at 1.69 V (vs. RHE). It shows that HMF conversion, FDCA yield, reaction time and FE of FDCA are 96.4%, 80.3%, 206 min and 80.5%, respectively, in Table S1. However, when CuO NWs/CuF was used as anode electrode at 1.64 V (vs. RHE), which is more negative by 50 mV than the potential used for $Cu(OH)_2$ NWs/CuF, there was 99.4% of HMF conversion with 90.9% yield and 90.4% FE of FDCA after 89 min. The detailed product distribution with HMF conversion as following charge passed in electrochemical cell is shown in Fig. 5(a). Since the HMF oxidation follows two pathways to converting as FFCA, one is the DFF pathway and the other is HMFCA pathway; both DFF and

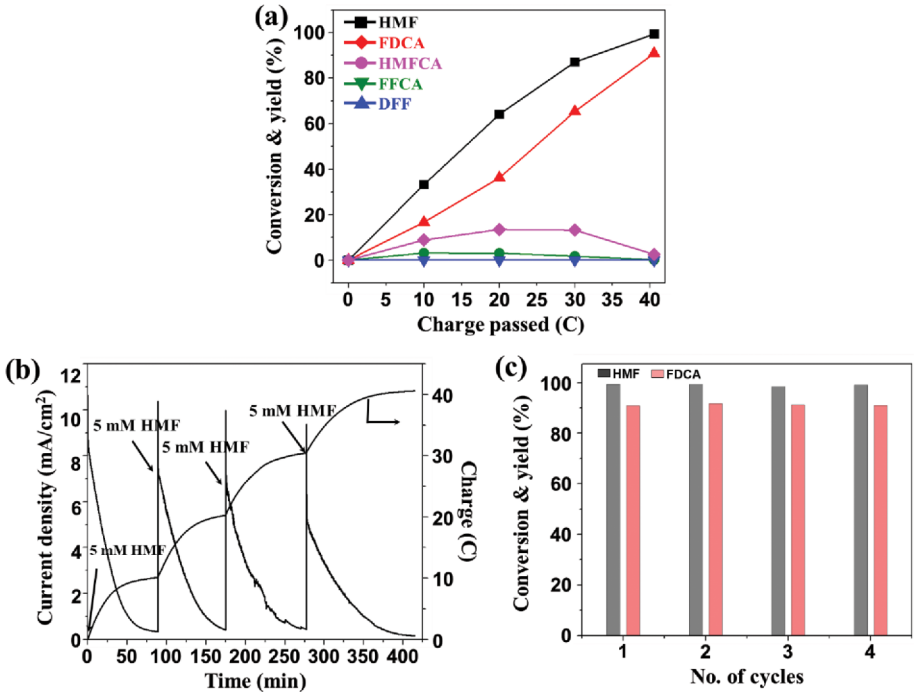

Fig. 5. Electrocatalysis of HMF oxidation into FDCA. (a) Changes in the HMF conversion (%) and its production yields (%) obtained by CuO NWs/CuF anode at 1.64 V vs. RHE. (b) Multiple oxidation steps involved in the conversion of HMF into FDCA. (c) HMF conversion (%) and yield of FDCA for four consecutive HMF oxidation.

HMFCA were detected as product. However, it is noticeable that the yield of HMFCA is much higher than that of DFF during electrolysis, which indicates that the first step of HMF oxidation by CuO NWs/CuF under the designated potential mainly follows pathway (b) in Scheme S1 [32]. Also, the FFCA concentration is negligible during electrolysis, which suggests that the conversion rate of FFCA to FDCA is much faster than the formation rate of FFCA from HMFCA. These results clearly indicate that CuO NWs/CuF had the best kinetic and thermodynamic properties for HMF oxidation and led to remarkable HMF oxidation into FDCA compared to that obtained using $Cu(OH)_2$ NWs/CuF.

The recyclability of CuO NWs/CuF electrode was investigated by adding fresh HMF several times in an electrochemical cell during reaction. As upon an addition of fresh 5 mM of HMF solution as a reactant, reaction current was recovered immediately during four-times of HMF addition, which means that CuO NWs/CuF was stable in reaction and maintained electrocatalytic activity on HMF oxidation during repeated reaction cycles (Fig. 5(b)). The CuO NWs/CuF electrode maintained high electrocatalytic properties in repeated cycles of HMF oxidation, showing over ~90% of FDCA yield (Fig. 5(c).

Because the electrochemical HMF oxidation reaction is accompanied by hydrogen evolution reaction as water reduction reaction, the amount of produced hydrogen in cathodic compartment is also measured by GC. The amount of generated hydrogen is consistent with theoretically calculated hydrogen amount based on passed charge during HMF oxidation reaction, which means that almost 100% of FE for hydrogen production was achieved (Fig. S3).

CONCLUSION

Free-standing $Cu(OH)_2$ and CuO NWs/CuF as electrode were prepared by inorganic polymerization and dehydration to study the electrochemical activity of HMF oxidation. Transforming from $Cu(OH)_2$ to CuO, CuO NWs/CuF (0.28 Cu atoms/nm^2) has threefold enhanced number of Cu atoms in the unit surface areas compared to $Cu(OH)_2$ NWs/CuF (0.09 Cu atoms/nm^2). The large amount of Cu atoms on the surface of electrode exhibits not only the required lowest applied potential but increased electron transfer rate for HMF oxidation reaction. Furthermore, CuO NWs/CuF retained over ~90% of FDCA yield over four cycles of reaction. These results provide an approach for the rational design of highly active catalyst on porous electrode for the electrochemical HMF oxidation into FDCA and hydrogen production under aqueous solution.

ACKNOWLEDGEMENTS

This work was supported by Basic Science Research Program (NRF-2019R1C1C1004210) through the National Research Foundation of Korea (NRF) grant funded by the Ministry of Science, ICT and Korea Research Institute of Chemical Technology (KRICT) core project (SI1941-20).

SUPPORTING INFORMATION

Additional information as noted in the text. This information is available via the Internet at http://www.springer.com/chemistry/journal/11814.

REFERENCES

1. J. J. Bozell and G. R. Petersen, *Green Chem.*, **12**, 539 (2010).
2. A. J. J. E. Eerhart, A. P. C. Faaij and M. K. Patel, *Energy Environ. Sci.*, **5**, 6407 (2012).
3. A. Corma, S. Iborra and A. Velty, *Chem. Rev.*, **107**, 2411 (2007).
4. B. Agarwal, K. Kailasam, R. S. Sangwan and S. Elumalai, *Renew. Sustain. Energy Rev.*, **82**, 2408 (2018).
5. Z. Zhang and K. Deng, *ACS Catal.*, **5**, 6529 (2015).
6. S. E. Davis, L. R. Houk, E. C. Tamargo, A. K. Datye and R. J. Davis, *Catal. Today*, **160**, 55 (2011).
7. X. Liu, J. Xiao, H. Ding, W. Zhong, Q. Xu, S. Su and D. Yin, *Chem. Eng. J.*, **283**, 1315 (2016).
8. N. Li, S. Tang and X. Meng, *J. Mater. Sci. Technol.*, **31**, 30 (2015).
9. H. Ait Rass, N. Essayem and M. Besson, *ChemSusChem*, **8**, 1206 (2015).
10. H. G. Cha and K.-S. Choi, *Nat. Chem.*, **7**, 328 (2015).
11. L. Özcan, P. Yalçın, O. Alagöz and S. Yurdakal, *Catal. Today*, **281**, 205 (2017).
12. N. Jiang, B. You, R. Boonstra, I. M. Terrero Rodriguez and Y. Sun, *ACS Energy Lett.*, **1**, 386 (2016).
13. X. Tong, L. Yu, H. Chen, X. Zhuang, S. Liao and H. Cui, *Catal. Commun.*, **90**, 91 (2017).
14. Y.-B. Huang, M.-Y. Chen, L. Yan, Q.-X. Guo and Y. Fu, *ChemSusChem*, **7**, 1068 (2014).
15. M. J. Kang, H. Park, J. Jegal, S. Y. Hwang, Y. S. Kang and H. G. Cha, *Appl. Catal. B*, **242**, 85 (2019).
16. Y. Feng, T. Jiao, J. Yin, L. Zhang, L. Zhang, J. Zhou and Q. Peng, *Nanoscale Res. Lett.*, **14**, 78 (2019).
17. F. Zhan, R. Wang, J. Yin, Z. Han, L. Zhang, T. Jiao, J. Zhou, L. Zhang and Q. Peng, *RSC Adv.*, **9**, 878 (2019).
18. X. Wen, W. Zhang and S. Yang, *Langmuir*, **19**, 5898 (2003).
19. C.-T. Hsieh, J.-M. Chen, H.-H. Lin and H.-C. Shih, *Appl. Phys. Lett.*, **82**, 3316 (2003).
20. Z. Li, Y. Chen, Y. Xin and Z. Zhang, *Sci. Rep.*, **5**, 16115 (2015).
21. W. Zhang, X. Wen and S. Yang, *Inorg. Chem.*, **42**, 5005 (2003).
22. C. Kim, K. M. Cho, A. Al-Saggaf, I. Gereige and H.-T. Jung, *ACS Catal.*, **8**, 4170 (2018).
23. H. Ming, K. Pan, Y. Liu, H. Li, X. He, J. Ming, Z. Ma and Z. Kang, *J. Cryst. Growth*, **327**, 251 (2011).
24. P. Wang, C. Qi, L. Hao, P. Wen and X. Xu, *J. Mater. Sci. Technol.*, **35**, 285 (2019).
25. L. Meng, W. Tian, F. Wu, F. Cao and L. Li, *J. Mater. Sci. Technol.*, **35**, 1740 (2019).
26. J. Huang, H. Li, Y. Zhu, Q. Cheng, X. Yang and C. Li, *J. Mater. Chem. A*, **3**, 8734 (2015).
27. M. J. Kang and Y. S. Kang, *J. Mater. Chem. A*, **3**, 15723 (2015).
28. C.-C. Hou, W.-F. Fu and Y. Chen, *ChemSusChem*, **9**, 2069 (2016).
29. I. G. Casella and M. Gatta, *J. Electroanal. Chem.*, **494**, 12 (2000).
30. J. Yu and J. Ran, *Energy Environ. Sci.*, **4**, 1364 (2011).
31. W. H. Leng, Z. Zhang, J. Q. Zhang and C. N. Cao, *J. Phys. Chem. B*, **109**, 15008 (2005).
32. O. Casanova, S. Iborra and A. Corma, *ChemSusChem*, **2**, 1138 (2009).